High-Throughput Refractive Index-Based Microphotonic Sensor for Enhanced Cellular Discrimination

Antoine Leblanc-Hotte[a,*], Geneviève Chabot-Roy[b], Livia Odagiu[b,c], Manon Richaud[d], Sylvie Lesage[b,c], Jean-Sébastien Delisle[d,e,f], Yves-Alain Peter[a]

[a] *Department of Engineering Physics, Polytechnique Montreal, 2500, Chemin de Polytechnique, Montreal, Québec, Canada, H3T 1J4*
[b] *Cellular Immunogenetics Laboratory, Maisonneuve-Rosemont Hospital Research Center, 5415, Boulevard de l'Assomption, Montreal, Québec, Canada, H1T 2M4.*
[c] *Département de microbiologie, infectiologie et immunologie, Université de Montréal, C.P. 6128, succursale Centre-ville, Montreal, Québec, Canada, H3C 3J7.*
[d] *Cancer and Transplantation Immunology Laboratory, Maisonneuve-Rosemont Hospital Research Center, 5415, Boulevard de l'Assomption, Montreal, Québec, Canada, H1T 2M4.*
[e] *Department of medicine, Université de Montréal, C.P. 6128, succursale Centre-ville, Montreal, Québec, Canada, H3C 3J7.*
[f] *Hemato-oncology service, Maisonneuve-Rosemont Hospital, 5415, Boulevard de l'Assomption, Montreal, Québec, Canada, H1T 2M4.*

Abstract

This paper presents a novel microphotonic sensor based on silicon technologies for high-throughput single cell measurements. It employs a highly sensitive Fabry-Pérot resonant cavity to extract cellular refractive index information. The integrated large cross-section rib waveguides provide a single-mode like behavior important for resonant cell sensing. Differentiated myeloid cells derived from a promyelocytic leukemia cell line were injected in a microchannel, sheathlessly focused using inertial forces and analyzed while flowing through the resonant cavity volume. Results were compared against a commercial flow cytometer and showed a substantial improvement on cellular discrimination. Thus, this sensor has the ability to discriminate cell populations, usually identified using fluorescent parameters, without any dyes and can reach measurement rate as high as 2000 cells per second. By harnessing the cell's effective volume refractive index, our device offers complementary measurements readily improving actual technologies and thus providing crucial information for research and clinical professionals.

Keywords: Microphotonic, Fabry-Pérot, Optical microcavity, Refractive index, Microfluidic, Cell sorting, Sensor

1. Introduction

Complete blood counts are essential to monitor a patient general health by measuring the number and quality of white blood cells, red blood cells and platelets. These tests performed in many hospitals and research centers rely on hematology analyzers which include flow cytometers and Coulter counters. While the Coulter principle is an electrical impedance measurement used to count the types of cells, flow cytometry uses interaction of light with cells to qualify their type. Owing to its measurement rate in the order of 10 000 cells per second, it is a tool of choice amongst clinical and research professionals.

In flow cytometry, cells are tightly focused in a fluid stream and cross a perpendicular laser beam. Detectors placed at strategic angles measure Forward Scattered Light (FSC) and Side Scattered Light (SSC). Forward Scattered light is influenced by the size of the cell and Side Scattered light is influenced by the granularity of the cell. FSC/SSC measurements are mainly used to identify living cells and exclude dead cells or doublets. Furthermore, flow cytometers constantly improve their selectivity using fluorescent parameters [1]. Pretreatment with an antibody-fluorophore complex targets specific features of the cells while monochromatic lasers optically excite each individual type of complex on their flowing course. Expression levels of these specific features are fundamental to medical professionals diagnostic and interpretation. Polychromatic flow cytometry can now yield 20 to 30 different fluorescent channels owing to the conjunction of quantum dots and organic fluorophores [2–4] and major manufacturing companies are aiming to reach 50 channels in a near future. However, these dyes can be very expensive, the necessary pretreatment procedures can be time consuming in addition to increase cell death and measurements need carefully calibrated software compensations to account for overlapping fluorescence spectra. Additionally, benchtop flow cytometers have a high cost, are space consuming, lack portability and require trained operating personnel.

On the other hand, numerous integrated miniaturized flow cytometers measuring scattered light, fluorescence or attenuation, have been developed to mimic their benchtop equivalent in a point-of-care manner [5–10]. These minia-

*Corresponding author
Email address: antoine.leblanc-hotte@polymtl.ca (Antoine Leblanc-Hotte)

turized systems are a promising alternative considering their lower cost and portability. Although reporting very good performances, these systems measure the same physical and fluorescent parameters as flow cytometry. However, the integration of microphotonics and microfluidics components on a single device can harness different cellular physical properties. In particular, refractive index of single cells has attracted a lot of interest recently and fueled recent microsystems developments. Microfabricated surface refractometers using whispering gallery modes in different configurations [11–13], photonic crystal cavities [14], surface plasmon resonance [15] and evanescent wave interaction in gratings [16] or interferometers [17] reported high sensitivity and resolution around 10^{-6} to 10^{-8} Refractive Index Unit (RIU) but they all lack depth of interaction required for whole cell characterization. Microfabricated Fabry-Pérot resonators are sensitive to the medium inside their cavity and thus are good volume refractometer candidates, even if reporting lower resolution around 10^{-5} RIU [18–20].

Whole cell refractive index analyses were reported previously using forward scattered light from two-beam laser trap [21], an external laser resonant cavity [22] and optical fiber Fabry-Pérot cavities [23, 24]. In these studies, single effective refractive index is used as critical parameter to identify various cancer cells from the kidney, cervix, adrenal medulla, breast and lymphocytes. It has also been shown by others that the refractive index could help diagnose certain infections, malaria and anemia [25]. Another study reported an out-of-plane integrated Fabry-Pérot cavity using cell-generated secondary optical transverse modes to differentiate lymphoma from lymphocytes with high specificity and sensitivity [26]. Although providing important information on a cell's refractive index related to its state or specific pathology, no dynamic or high-throughput measurement of large cellular population have been demonstrated by any of these microsystems.

Nevertheless, there is a high demand amongst biomedical technologists for use and improvements in polychromatic flow cytometry equipment. Clinical and research professionals both strive to obtain cutting-edge technologies that offer high-throughput, multiparametric and diversified single-cell measurement, ideally in a single system. The proposed device directly mitigates this shortcoming by offering new non-fluorescent discrimination parameter in a high-throughput manner. This report presents a novel microphotonic sensor based on silicon technologies for high-throughput single cells measurement. It employs a highly sensitive Fabry-Pérot resonant cavity, $\Delta n = 1.6 \times 10^{-5}$, reported in previous work [20, 27, 28] to extract cellular refractive index information. The integrated large cross-section rib waveguides provide a single-mode like behavior important for resonant cell sensing [20]. Differentiated myeloid cells derived from a promyelocytic leukemia cell line were injected in a microchannel, sheathlessly focused using inertial forces and analyzed while flowing through the resonant cavity volume. This dynamic measurement of a cell's effective volume refractive index enables new parameters for cellular population discrimination. Furthermore, this microsystem does not require any dye treatment of the cells, accepts any cell shape and can reach measurement rate of 2000 cells per second. Results were compared against a commercial flow cytometer and showed a substantial improvement on cellular population discrimination. Indeed, FSC-SSC based flow cytometry could not distinguish between any of the three differentiated myeloid cells populations whereas the microsystem could distinguish two of these cell types. We believe such microphotonic system represents an important step towards distinguishing different cell types and could be integrated in flow cytometry instruments and cell counter devices.

2. Materials and methods

2.1. Microfabrication

The device was fabricated by conventional silicon micromachining using photolithography and Deep Reactive Ion Etching (DRIE) as core processes. We used a Silicon-On-Insulator (SOI) wafer comprising a handle layer of 600 μm, a Buried Oxide (BOX) layer of 0.5 μm and a device layer of 15 μm. First, microfluidic channels and Distributed Bragg Reflectors (DBRs) were patterned using a positive photoresist. DBRs were designed according to previously published work [28] to achieve a Fabry-Pérot cavity with resonances in the Near Infrared (NIR) region. These structures were etched in the silicon device layer down to the BOX using a DRIE-BOSCH process with alternating SF_6 and C_4F_8 plasmas. Then, similarly, rib waveguides were photolitographically defined and etched to a lower height. Microstructured SOI wafers were cut into separate chips using a dicing saw (ADT, Provectus 7100) and an engineered resin/diamond blade for optical quality facets with low scattering losses. This dicing method previously reported a mean roughness value of 5.5 *nm* [20]. Manufactured and diced Pyrex plates with holes of 760 μm in diameter were anodically bonded on top of the chips to seal the microfluidic channels. Tygon microbore tubings were then connected to the microchannels entries and exits and bonded using ultraviolet reactive glue. Figure 1a shows a 3D rendering of the assembled microphotonic cell sensor device and Fig. 1b reports a scanning electron microscopy (SEM) image of the fabricated device showing the rib waveguides, DBRs, Fabry-Pérot cavities and microfluidic channel. Verticality of DBRs trenches were measured using transverse SEM images and reported a value of $90.0 \pm 0.2°$.

2.2. Single-mode like Rib waveguide

Geometries of the rib waveguides were designed according to previously published work to yield a single-mode like propagation [20]. Briefly, we calculated higher order

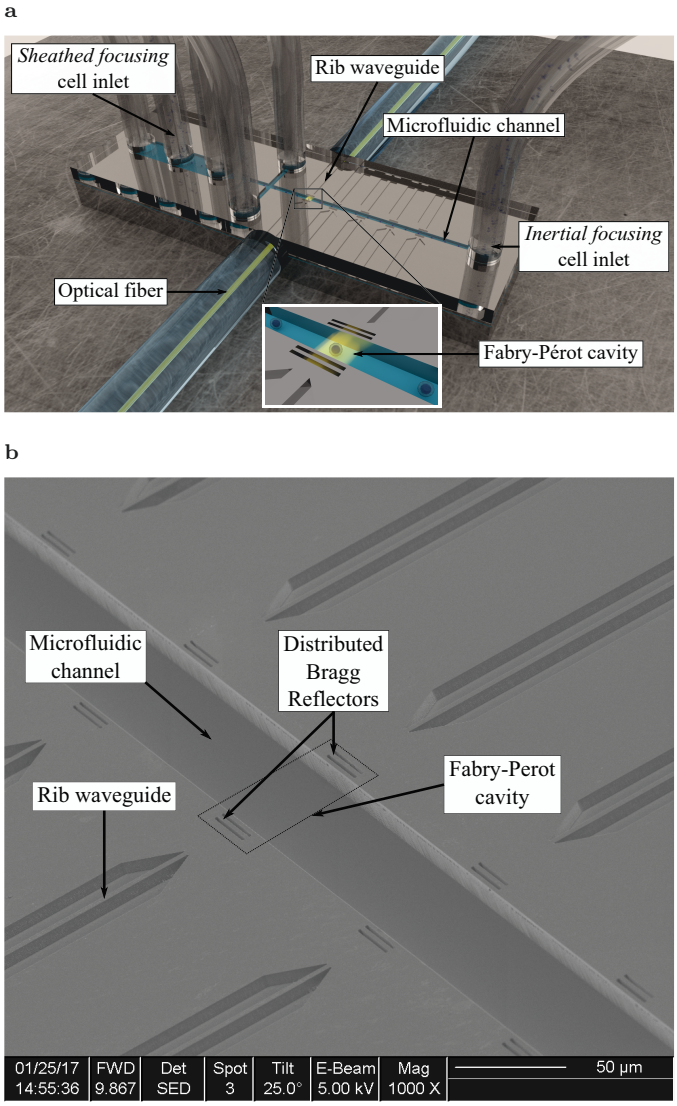

Fig. 1. Illustrations of the microphotonic cell sensor with (a) 3D rendering of the assembled device using Blender Software and (b) SEM image of the microfabricated rib waveguides, DBRs, Fabry-Pérot cavities and microfluidic channel.

optical modes attenuations for several rib waveguide dimensions at different wavelengths. We used a Finite Difference method and a direct matrix solver with Perfectly Matched Layers as boundary conditions to compute supported modes. The imaginary part of the complex refractive index for each computed mode, *i.e.* the extinction coefficient, was converted into an attenuation coefficient. This technique yielded an attenuation map showing regions of interest corresponding to single-mode like behavior. Figure 2 shows the combined attenuation map for modes HE_{10}, HE_{20}, HE_{30} and HE_{40} at wavelengths of $\lambda = 1.50\ \mu m$, $1.575\ \mu m$ and $1.65\ \mu m$ with onsets showing a schematic of the rib waveguide cross-section with corresponding variables and the single-mode like NIR output mode profile of a $5.5\ \mu m$ rib waveguide after $5.85 \pm 0.01\ mm$ of propagation. Experimental setup used to analyze the NIR output mode profile is described in *Section 2.5*. Fabricated rib waveguides were chosen to be $5.0\ \mu m$ and $5.5\ \mu m$ in width and $9.5\ \mu m$ in height, represented by the white dots in Fig. 2.

2.3. Microfluidic operation

Samples injection were made using a syringe pump (Harvard Apparatus, Pump 11 Pico Plus Elite) connected to the inertial focusing cell inlet tube (Fig. 1a) at a flow rate of $5\ \mu l/min$.

It is worth mentioning that since the resonant cavity does not have a focal point, position of cells along the width of the microchannel had a negligible impact on the output signal. Nevertheless, the two-stages sheathless inertial focusing as reported by Zhou and Papautsky will affect cells position flowing through the microchannel [29]. Indeed, particles flowing through a rectangular microchannel will focus to four distinct lateral equilibrium positions due to the inertial lift forces involved, the shear-induced lift force, the wall-induced lift force and the rotation-induced lift force. In the first stage, fast migration of cells toward channel walls is caused by the shear-induced and wall-induced lift forces balance whereas in the second stage slow migration of cells to center points of walls is caused by the rotation-induced lift force. This is true for confined flows at finite Reynolds number. However, with increasing channel aspect ratio, equilibrium positions on short faces disappear leaving only two equilibrium positions centered at the long face of the channel. For flowing lengths higher than the complete focusing length, cells will remain focused to the equilibrium positions and ordered with preferred interparticle spacing [30]. The complete focusing length required for particle migration is

$$L = \frac{3\pi\mu {D_h}^2}{4\rho U_f a^3}\left(\frac{H}{{C_L}^-} + \frac{W}{{C_L}^+}\right), W > H \qquad (1)$$

where μ and ρ are the fluid viscosity and density, D_h is the hydraulic diameter, U_f is the average flow velocity, a is the particle diameter, H and W are the channel height and width respectively and ${C_L}^-$ and ${C_L}^+$ are the negative and positive lift coefficients estimated through the authors data. ${C_L}^-$ is associated to the migration away from the center points of walls (fast migration in stage I) and ${C_L}^+$ is associated to the migration toward the center points of walls (slow migration in stage II). In the present study the microchannel dimensions are $H = 15\ \mu m$ and $W = 35\ \mu m$, cell diameter is $12\ \mu m$, flow rate is $Q = 5\ \mu l/min$ and fluid properties are approximated to the ones of water. ${C_L}^-$ is estimated to be 0.19 and ${C_L}^+$ estimated to 0.023. This yields a complete focusing length $L = 6\ mm$. The cavity used in this study was placed $1.2\ mm$ away from the inlet. Thus, cells will be partially focused around the equilibrium positions with a spread of $29\ \mu m$ in the direction of the width. Larger cells require less length to be completely focused, as shown in Eq. 1. This might lead larger cells to yield a less scattered population and thus create

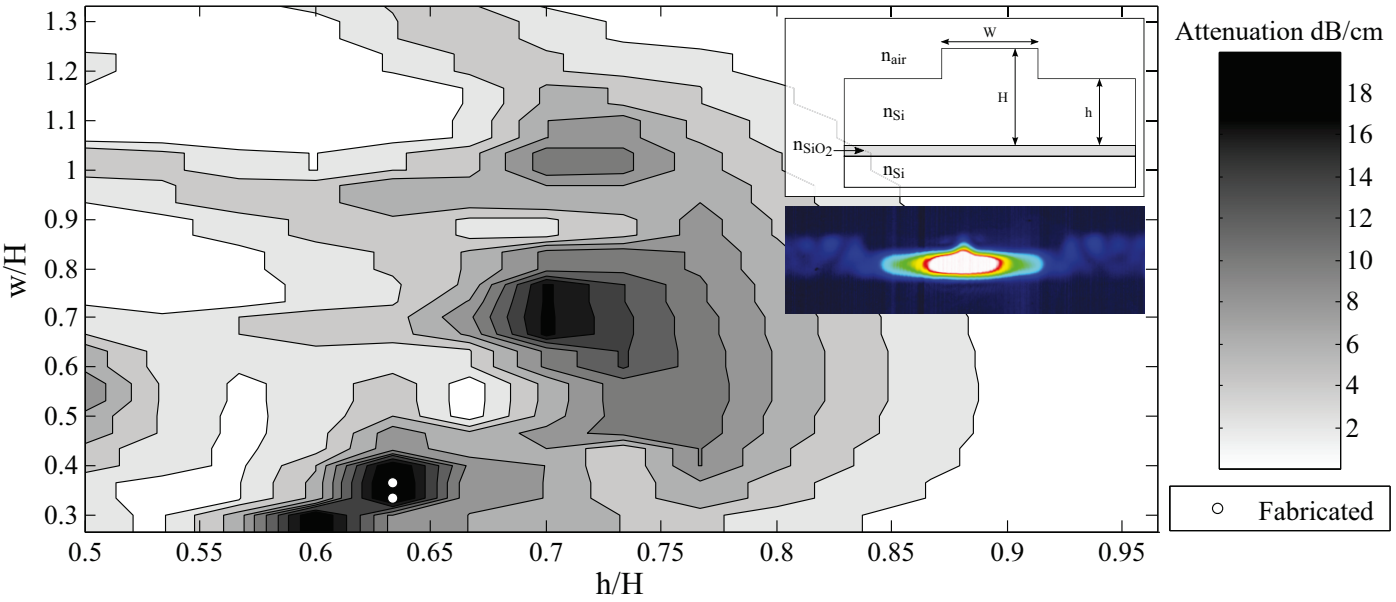

Fig. 2. Combined attenuation map for modes HE_{10}, HE_{20}, HE_{30} and HE_{40} at wavelengths of $\lambda = 1.50\ \mu m$, $1.575\ \mu m$ and $1.65\ \mu m$. Onsets showing a schematic of the rib waveguide cross-section with corresponding variables and the single-mode like NIR output mode profile of the fabricated $5.5\ \mu m$ rib waveguide.

an inertial focusing contribution to the discrimination capability of the device. However, cell with the same size distributions, as for these experiments, will behave similarly. Furthermore, since planar DBRs are used, the sensing cross-section of the optical resonant profile is uniform along the cavity axis. Thus, position of the cells in this axis should have negligible impact on the output signal. Lateral hydrodynamic focusing used in a previous device [31] does not suggest a significant difference on population spreading compared to inertial focusing. Still, devices were designed with multiple entries as shown in Fig. 1a to keep open the possibility of sheathed 3D hydrodynamic focusing when cells were too small to be confined in height solely by this phenomenon.

2.4. Cell culture

The HL-60 cell line was obtained from the ATCC (#CCL-240), maintained in RPMI containing 20% Fetal Calf Serum (FCS) and kept in a humid chamber at 37°C with 5% CO_2. HL-60 is a promyelocytic leukemia cell line that can be differentiated into various myeloid cell types depending on the culture condition. We opted to differentiate the HL-60 cells into basophils and neutrophils. HL-60 cells were passaged in differentiation media, in RPMI containing 10% FCS with 1% HEPES (baseline condition). To obtain neutrophils, 2×10^5 HL-60 cells per ml were cultured with 1.25% dimethylsulfoxide (DMSO, Sigma) for seven days [32]. To obtain basophils, 2×10^5 HL-60 cells per ml were maintained for seven days in the absence of serum [33].

At day 7 of culture, the HL-60 cells were harvested, washed in phosphate buffered saline (PBS) containing 2% FCS and 1 mM EDTA. The cells were counted and resuspended in PBS (2% FCS, 1 mM EDTA) at a concentration of 2 million cells per ml. Cell aggregation is prevented using 1 mM EDTA (Ethylenediaminetetraacetic acid) a known chelating agent binding to calcium and hindering calcium specific adhesion (cadherins) and thus preventing cell clumping. Nevertheless, cell aggregation can still occur. In both the flow cytometer and microphotonic sensor, data from small cell clusters are readily excluded by the amplitude or width of the signal, whereas larger cell clusters tend to block the device, which must then be cleaned prior to further data acquisition. Samples where cell viability was below 50% were excluded from further analyses. 150 000 cells were placed on a slide by cytospin and subjected to Wright-Giemsa staining. The data was acquired on a microscope (Zeiss, AxioImager Z2) using a 63X oil immersion objective. All solutions were divided into two separate tubes, one for data acquisition with flow cytometry and one for data acquisition with the microsystem.

2.5. Experimental setups

In this study, three different experimental setups were used: one to analyze the NIR output mode profile, one to analyze the spectral response from the rib waveguides alone as well as coupled to the Fabry-Pérot cavity and finally one to register optical power variation in time at a fixed wavelength for single cell analysis.

NIR mode profile of rib waveguides were assessed using a standard SMF-28 fiber butt coupling light from a wide band laser source (Newport, BBS-430) in the inlet facet. Outputted light was collected on an InGaAs camera (VDS Vosskhler GmbH, NIR-610PGE) through an objective lens using a 45°angled mirror. For the spectral analysis setup, an optical spectrum analyzer (Hewlett Packard,

86142A) collected the outputted NIR light through a butt coupled optical fiber and recorded the normalized spectrum. The raw spectrum was normalized using the wide band laser source as a reference. Stand-alone rib waveguides and Fabry-Pérot coupled rib waveguides were assessed. Certified refractive index oils were used to measure the resonance peak sensitivity. The optical power variation measurement setup fixed the propagating wavelength at the top of the Fabry-Pérot resonance using a tunable laser source(Agilent, 8164B). As a cell flew through the Fabry-Pérot cavity, the resonance peak shifted towards longer wavelength because the refractive index of the cell is higher than the surrounding liquid (PBS). A fast InGaAs infrared photodetector (Thorlabs, DET01CFC) recorded optical power variations at the output and relayed it to a high speed digitizer (National Instruments, NI-PXI 5114). A LabView program was developed to allow for fast acquisition of the relayed voltage variation in time.

2.6. Flow cytometry measurements

Three sub-parameters, height, width and area, were automatically extracted from FSC and SSC measurements. 50 000 cells of the basophils and neutrophils solutions were processed for data acquisition on the same BDCANTO flow cytometer. Flow cytometry samples were analyzed using FlowJo software. *Overlaprate* (ORL) coefficients were computed in parallel using equation 2, as detailed below.

2.7. Single cell analysis

Distinctively from FSC and SSC, sensor measurements are influenced by the effective volume refractive index of the cells. Single cell curves were analyzed and compared against each others based on multiple extracted parameters using a custom made MatLab visualization algorithm. As for flow cytometry, *overlaprate* (ORL) coefficients were computed in parallel using equation 2.

To confirm that two scatter populations, *i.e.* clusters, are indeed distinguishable we computed the *overlaprate* (ORL) coefficient as reported by Sun and Wang in equation 2 [34]. This coefficient is calculated as the ratio of the probability density function (PDF) value at the saddle point and the PDF value at the lowest local maximum. Authors also developed an algorithm to find the saddle point of the PDF in any number of dimensions. Essentially, it solves a set of differential equations allowing to find a curve which always contains the maxima and saddle point. Qualitatively, two cluster are well separated if the ORL is less than 0.6, partially overlapping in the interval [0.6, 0.8] and strongly overlapping if greater than 0.8. A value of 1 indicates that no saddle point could be found and that the two clusters are completely overlapping.

$$ORL = \frac{p(X_{Saddle})}{p(X_{Submax})} \tag{2}$$

We computed the ORL by fitting a Gaussian distribution over each measured cell population for each parameter and applied an affine transformation on the entire set of data to simultaneously diagonalize both population's covariance matrices [35]. Using this technique gave us a set of real functions with a single dependent variable in each one. However, extracted parameters are correlated in the same population since there is only one physical measurement, i.e. the displacement of the resonance peak in time. We found that a 4 to 5 dimension PDF gave us enough precision to asses clusters separation while minimizing the computing error due to the simultaneous diagonalization of these correlated parameters. In particular, parameters that do not have linear covariances, such as height, width and area altogether in FSC or SSC, are badly approximated by a Gaussian distribution. Thus, height subparameters were excluded from the ORL computation.

3. Results and discussion

3.1. Single-mode like Rib Waveguides

Spectral measurements of the 5.0 μm and 5.5 μm rib waveguides for propagation lengths of 5.85, 7.35, 9.85 and 15.84 mm reported total coupling losses of -15.5 dB and propagation losses ≤ 1.5 dB/cm for both width. Intensity variation along wavelengths between $\lambda = [1475,\ 1675]$ nm reported a mean standard deviation of 0.9 dB and 0.8 dB for rib widths of 5.0 μm and 5.5 μm respectively. Based on these results and the NIR output mode profile shown in Fig. 2, fabricated rib waveguides built from the theory developed in previous work [20] are indeed single-mode like.

3.2. Resonant cavity sensing

Figure 3a shows the experimental spectrum of the Fabry-Pérot cavity with DBRs widths of 2.0 μm, microchannel width of 35 μm and rib waveguide width of 5.5 μm. The red line represents the wavelength at which the tunable laser was locked for optical power variation measurements.

Noticeably, the spectrum presents two distinct peaks per expected resonance. Further experiments are necessary to precisely determine the underlying phenomena responsible for these "double peaks". However, Finite Difference simulations results yielded fundamental TE and TM modes propagating with slightly different modal indices $\Delta n \sim 5 \times 10^{-5}$ ($n_{TM} < n_{TE}$), attenuation coefficients $\Delta\alpha \sim 0.25$ dB/cm ($\alpha_{TM} < \alpha_{TE}$) and mode sizes ($size_{TM} < size_{TE}$). Additionally, standard optical transfer matrix simulations with an incident Gaussian beam revealed that two-period DBRs (air-silicon-air-silicon) better fits the resonance's FWHM, *i.e.* the overall reflectivity of the DBRs. Furthermore, these "double peaks" can be well fitted with cavity gaps of different optical lengths. The best fit was found for cavities having a geometrical length difference of 115 nm and a refractive index difference of 5×10^{-5} RIU. Thus, it is reasonable to consider that TE and TM modes would exhibit distinct peaks in the

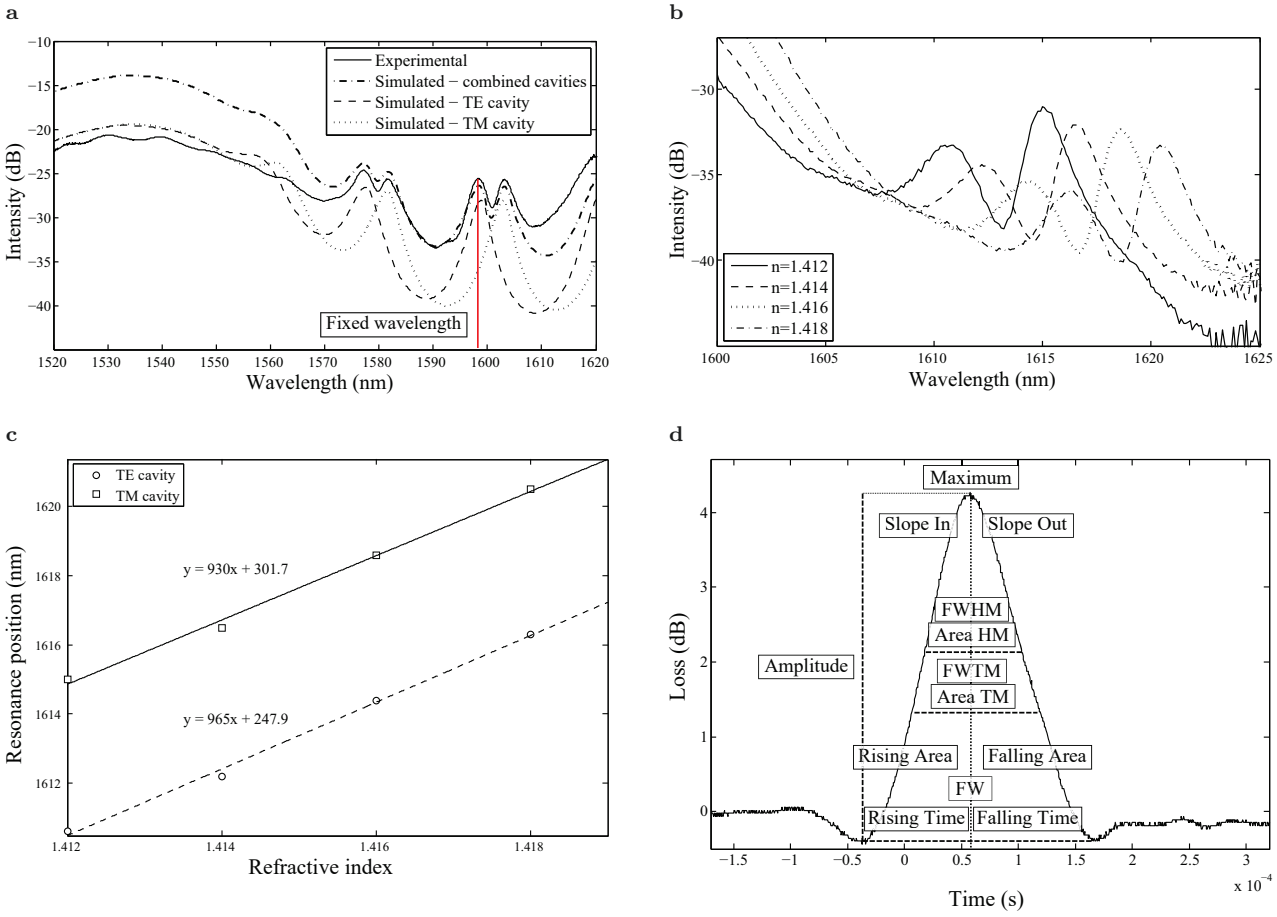

Fig. 3. (a) Experimental spectrum of the Fabry-Pérot cavity with DBRs widths of 2.0 μm, microchannel width of 35 μm and rib waveguide width of 5.5 μm (solid line) and simulated spectra for the TE cavity (dashed line), TM cavity (dotted line) and combined cavities (dashed-dotted line). (b) Superimposed spectra of the Fabry-Pérot resonance peaks shifts with corresponding refractive index value and (c) fitted linear regressions used to calculate the sensitivity of the *TE* and *TM cavities*. (d) Typical voltage variation in time curve for a single cell passage with corresponding extracted parameters.

spectrum due to the combined effect of their difference in modal index, attenuation coefficients and mode size. For future reference, we will use the term *"TE cavity"* to describe the resonances corresponding to a cavity gap with a higher refractive index and a shorter length whereas *"TM cavity"* will be for a cavity gap with a lower refractive index and a longer length. Simulated *TE* and *TM cavities* as well as their combination can be found in Fig. 3a. Deviation between experimental and simulated spectra can be partially justified when considering the effects of the rib waveguides. As reported previously, fabricated single-mode like rib waveguides do not yield an experimentally flat spectrum due to small energy transfer of the fundamental mode to higher optical modes [20]. Furthermore, simulations do not accommodate for multimode resonance in the cavity nor multimode coupling behavior with the optical fiber. Additionally, simulated roughness of the interfaces, approximated by an absorption layer, and effective thickness of the Bragg layers might differ slightly from the experimental device. Still, the overall simulated and experimental spectra are in good accordance.

Sensitivity and resolution were measured using a different cavity to avoid hindering by oil residue on the microchannel walls. Figure 3b shows the measured spectra with certified refractive index oils used to determine the resonance peaks shifts and Fig. 3c shows the linear regression fit used to calculate the *TE* and *TM cavities* sensitivities. Sensitivity and resolution values should be roughly the same between cavities since dimensions of DBRs and microchannels are very close and made simultaneously on the same SOI. Table 1 reports pertinent parameters of these cavities where FSR is the Free Spectral Range and the Finesse is calculated as $FSR/FWHM$. Resolution values were calculated considering a detection limit of $3\sigma = 0.015\ nm$ [20].

Figure 3d shows a typical signal in dB scale with the corresponding extracted parameters. FWHM is the Full Width at Half Maximum, FWTM is the Full Width at One Third of the Maximum, Area HM is the area under the curve at Half Maximum, Area TM is the area under the curve at One Third of the Maximum and FW is the Full Width. Supplementary computed parameters correspond

to the following ratios: Rising Time/Falling Time, Slope In/Slope Out, Rising Area/Falling Area, Maximum/FW, Maximum/FWHM, Maximum/FWTM, FWHM/FWTM, FWHM/FW and FWTM/FW. Considering a perfectly organized train of cells, the signal shown in Fig. 3d would repeat every 3 to 5×10^{-4} s, corresponding to rates of 3333 to 2000 cells/s respectively. The measurement rate is limited to these values due to the imposed flow rate of 5 $\mu l/min$. Higher flows will increase the velocity of cells in the cavity but cell deforming forces also rise. In particular, narrowing microchannels induce an elongation force which can rupture the cellular membrane above a certain threshold, thus limiting the operating flow rate.

Table 1: Fabry-Pérot resonances properties calculated from experimental spectra for the *TE* and *TM cavities*

	TE cavity	**TM cavity**
Loss at Maximum (dB)	-25.6	-25.7
FWHM (nm)	4.16	4.18
FSR (nm)	21.2	21.55
Finesse	5.1	5.2
Sensitivity (nm/RIU)	965	930
Resolution (RIU)	1.55×10^{-5}	1.61×10^{-5}

3.3. Promyelocytic leukemia biological model

The HL-60 cells were differentiated into neutrophils and basophils based on two distinct cell culture conditions. The efficacy of the differentiation was monitored by performing a Wright-Giemsa staining. Expectedly, the neutrophils exhibited segmented nuclei, while the basophils presented with vacuoles (Fig. 4d). As all samples presented distinct characteristics, we then aimed to determine if non-fluorescent parameters were sufficient to separate the cells by flow cytometry. As depicted in Fig. 4a, these cell culture conditions yielded cells with similar FSC-SSC profiles, such that they could not be readily discriminated by flow cytometry. Indeed, in the culture condition promoting neutrophil differentiation, the HL-60 cells tended to be a bit smaller and less dense than both undifferentiated cells and basophils. Still, overlay graphical representation of HL-60 in neutrophil promoting conditions over undifferentiated HL-60 cells (Fig. 4b blue vs green, respectively) or over HL-60 cells cultures in basophil-promoting conditions (Fig. 4c blue vs red, respectively) demonstrates that these conditions cannot be effectively separated based on either FSC or SSC and even when using both FSC and SSC as dot plot representation (Fig. 4a). To that effect, computed ORLs on flow cytometry data using equation 2 returned values of 1 for all combined cellular populations (see Table 2), validating that no discrimination could be established between these conditions.

On the other hand, microsystem measurements demonstrate a clear discrimination between some cellular populations. Fig. 4e shows baseline culture conditions, neutrophils and basophils solutions measured separately with the gated main population and bottom panel shows all combinations of these cellular populations. Discrimination occurs for baseline culture condition over neutrophil-differentiating conditions (Fig. 4f left, $ORL < 0.4$) as well as basophil- over neutrophil-differentiating conditions (Fig. 4f middle, $ORL < 0.4$). Discrimination between baseline culture condition over basophils-differentiating conditions could not be established (Fig. 4f right, $ORL = 1$). Axes on Fig. 4e and 4f were chosen for both simple association with optical power variation signal and better graphical visualization.

Table 2 reports the computed ORLs on each combination of HL-60 cellular populations for the flow cytometer and the microsystem. The parameters used to compute the flow cytometry ORL are FSC-A, FSC-W, SSC-A and SSC-W whereas the parameters for the microsystem ORL are FWHM, FWTM, Rising time, Falling time and FW in the first experiment and Maximum, FWHM, FW, Maximum/FW and Maximum/FWHM in the second experiment. Optimal ORL parameters are not exactly the same between experiments since the five linearly covariant parameters yielding the lowest ORL were chosen in each case. Thereupon, variation of biophysical properties between experiments as well as resonance peak profile variations due to re-coupling are factors inducing changes in optimal parameters for ORL computation. Nevertheless, cell populations with at least one two-parameter ORL less than 0.8 are always distinguishable whereas the ones with all two-parameters ORLs equal to 1 are never distinguishable, no matter which parameters are used. Conveniently, ORL parameters can be chosen for each set of experiments to palliate for variations without hindering the overall discrimination capability of the device. Consequently, FSC-SSC based flow cytometry could not distinguish between any of the HL-60 cells populations whereas the microsystem could distinguish between both neutrophil-differentiating conditions and undifferentiated HL-60 cells as well as neutrophil- and basophil-differentiating conditions in each experiment. Since FSC measurements reported no significant difference regarding the cell sizes, sensor measurements are confirmed to rely predominantly on the effective volume refractive index of the cells. These results confirm that our novel microphotonic sensor grants a substantial improvement on cellular population discrimination. It can be used complementarily to flow cytometry, enhancing its sorting capabilities, and thus provide crucial information for research and clinical professionals.

Table 2: ORL coefficients comparison between the flow cytometer and the microsystem for each experiment

	Flow cytometry		**Microsystem**	
Experiment	#1	#2	#1	#2
Baseline - Neutrophils	1	1	0.13	0.36
Basophils - Neutrophils	1	1	0.003	0.36
Baseline - Basophils	1	1	1	1

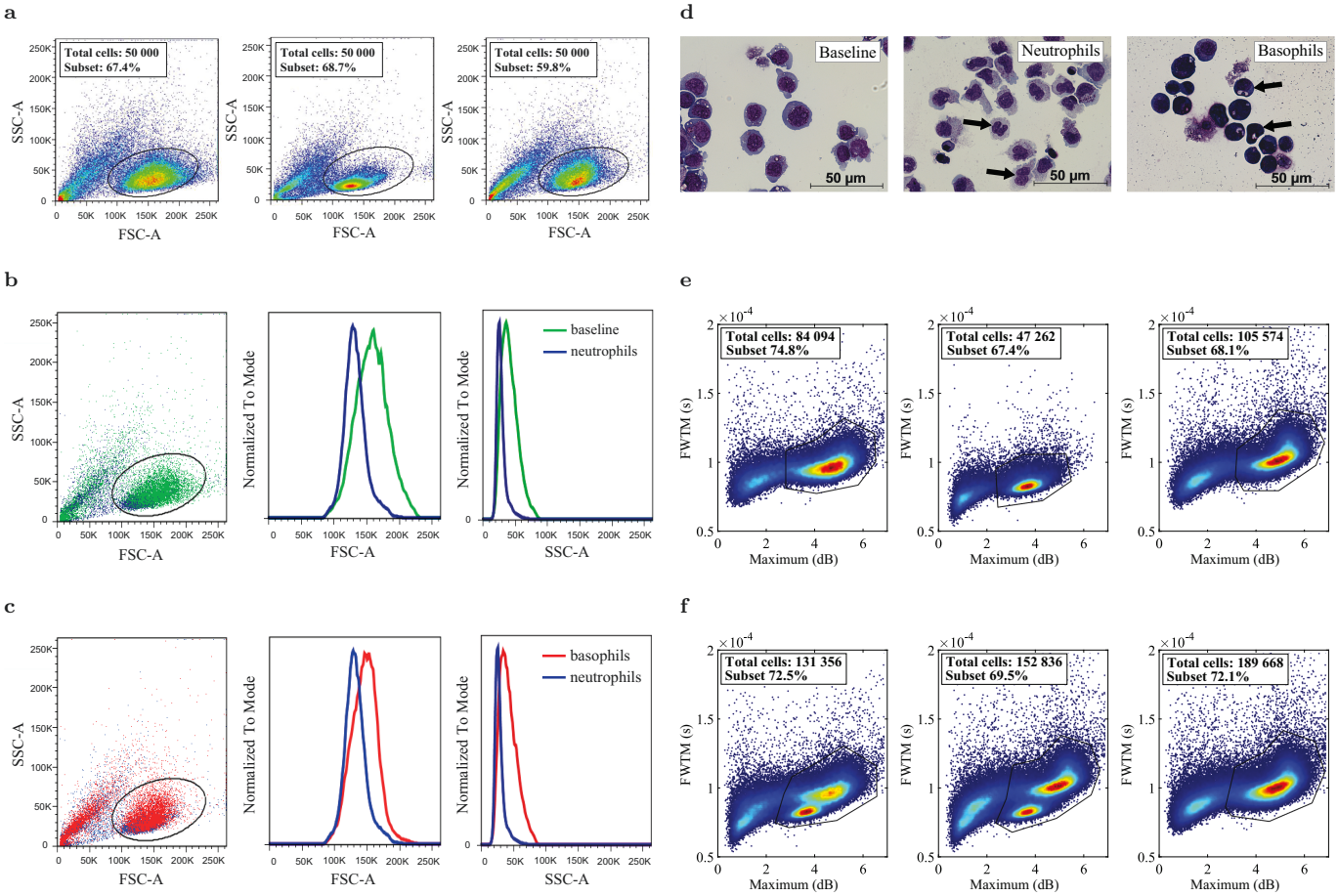

Fig. 4. HL-60 differentiated into basophils and neutrophils cannot be distinguished by typical FSC-SSC flow cytometry profiles. (a) Typical FSC-SSC profiles of HL-60 cells differentiated neutrophils (middle) or basophils (right). The baseline culture condition is also shown (left). The total number of measured cells and the percentage of gated cells is shown. (b) and (c) respectively depict overlays for baseline vs neutrophil-differentiating conditions and basophil- vs neutrophil-differentiating conditions; in dot plot (left), in FSC histogram (middle) and in SSC histogram (right) for baseline in green, neutrophils in blue and basophils in red. One representative of at least three experiments. (d) HL-60 cells were differentiated for 7 days into neutrophils (middle) or basophils (right). The baseline culture condition is also shown (left). Arrows on the right panel point to cells bearing vacuoles, typical of basophils, while arrows on the middle panel point to cells bearing a segmented nucleus characteristic of neutrophils. One representative of at least three experiments. (e) Color-coded density scatter plots in function of Maximum and FWTM for separately measured baseline culture conditions (left), HL-60 cells differentiated neutrophils (middle) and basophils (right) solutions and (f) combined cellular populations for baseline vs neutrophil-differentiating conditions (left), basophil- vs neutrophil-differentiating conditions (middle) and baseline vs basophil-differentiating conditions (right). The total number of measured cells and the percentage of gated cells is shown. One representative of at least two experiments.

4. Conclusion

We described a novel microphotonic system based on cellular refractive index measurement which represents an added value to actual cell counters and flow cytometry because of its improved ability to discriminate cell populations. Identification of HL-60 cells differentiated into neutrophils and basophils as well as a baseline culture was investigated and proved to be indistinguishable using FSC-SSC based flow cytometry while being distinguishable with our microsystem in the cases of baseline vs neutrophils and basophils vs neutrophils. Thus, this device represents an important step towards better cellular measurement capabilities. Furthermore, this microsystem does not require any dye treatment, accepts any cell shape and can reach measurement rate of several thousand cells per second.

Acknowledgments

The authors wish to thank the clinical hematology laboratory staff at Hôpital Maisonneuve-Rosemont for technical support with the Wright-Giemsa staining, the staff at Polytechnique Montreal's Laboratory of Microfabrication for technical support with microfabrication processes and Dr. Claire Viallard for technical support with imaging. This work is supported in part by the Natural Sciences and Engineering Research Council of Canada (NSERC) [grant number PGSD3-445848-2014], the Fonds de recherche du Québec – Nature et technologies (FRQNT) [grant numbers Equipe 173638 and RQMP 187779]. S. Lesage and J.-S. Delisle hold respectively a Senior and Junior II career award from the Fonds de recherche du Québec – Santé (FRQS).

References

[1] S. P. Perfetto, P. K. Chattopadhyay, M. Roederer, Seventeen-colour flow cytometry: unravelling the immune system., Nat. Rev. Immunol. 4 (2004) 648–655.

[2] P. K. Chattopadhyay, D. A. Price, T. F. Harper, M. R. Betts, J. Yu, E. Gostick, S. P. Perfetto, P. Goepfert, R. A. Koup, S. C. De Rosa, M. P. Bruchez, M. Roederer, Quantum dot semiconductor nanocrystals for immunophenotyping by polychromatic flow cytometry, Nat. Med. 12 (2006) 972–977.

[3] P. K. Chattopadhyay, T. M. Gierahn, M. Roederer, J. C. Love, Single-cell technologies for monitoring immune systems, Nat. Immunol. 15 (2014) 128–135.

[4] P. K. Chattopadhyay, M. Roederer, A mine is a terrible thing to waste: High content, single cell technologies for comprehensive immune analysis, Am. J. Transplant. 15 (2015) 1155–1161.

[5] M. Frankowski, J. Theisen, A. Kummrow, P. Simon, H. Ragusch, N. Bock, M. Schmidt, J. Neukammer, Microflow cytometers with integrated hydrodynamic focusing., Sensors 13 (2013) 4674–4693.

[6] X. Mao, A. A. Nawaz, S. C. S. Lin, M. I. Lapsley, Y. Zhao, J. P. McCoy, W. S. El-Deiry, T. J. Huang, An integrated, multiparametric flow cytometry chip using microfluidic drifting based three-dimensional hydrodynamic focusing, Biomicrofluidics 6 (2012) 24113.

[7] L.-M. Fu, Y.-N. Wang, Optical microflow cytometer based on external total reflection, Electrophoresis 33 (2012) 3229–3235.

[8] C.-H. Lin, G.-B. Lee, Micromachined flow cytometers with embedded etched optic fibers for optical detection, J. Micromech. Microeng. 13 (2003) 447–453.

[9] M. Rosenauer, W. Buchegger, I. Finoulst, P. Verhaert, M. Vellekoop, Miniaturized flow cytometer with 3D hydrodynamic particle focusing and integrated optical elements applying silicon photodiodes, Microfluid. Nanofluid. 10 (2011) 761–771.

[10] B. R. Watts, Z. Zhang, C. Q. Xu, X. Cao, M. Lin, Scattering detection using a photonic-microfluidic integrated device with on-chip collection capabilities, Electrophoresis 35 (2014) 271–281.

[11] F. Vollmer, S. Arnold, Whispering-gallery-mode biosensing: Label-free detection down to single molecules, Nat. Methods 5 (2008) 591–596.

[12] M. Iqbal, M. A. Gleeson, B. Spaugh, F. Tybor, W. G. Gunn, M. Hochberg, T. Baehr-Jones, R. C. Bailey, L. C. Gunn, Label-free biosensor arrays based on silicon ring resonators and high-speed optical scanning instrumentation, IEEE J. Sel. Top. Quantum Electron. 16 (2010) 654–661.

[13] S. M. Harazim, V. A. Bolaños Quiñones, S. Kiravittaya, S. Sanchez, O. G. Schmidt, Lab-in-a-tube: on-chip integration of glass optofluidic ring resonators for label-free sensing applications, Lab Chip 12 (2012) 2649.

[14] Y. N. Zhang, Y. Zhao, R. Q. Lv, A review for optical sensors based on photonic crystal cavities, Sens. Actuator A-Phys 233 (2015) 374–389.

[15] K. A. Willets, R. P. Van Duyne, Localized Surface Plasmon Resonance Spectroscopy and Sensing, Annu. Rev. Phys. Chem. 58 (2007) 267–297.

[16] G. Quero, A. Crescitelli, D. Paladino, M. Consales, A. Buosciolo, M. Giordano, A. Cutolo, A. Cusano, Evanescent wave long-period fiber grating within D-shaped optical fibers for high sensitivity refractive index detection, Sens. Actuator B-Chem. 152 (2011) 196–205.

[17] A. Ymeti, J. S. Kanger, J. Greve, G. A. Besselink, P. V. Lambeck, R. Wijn, R. G. Heideman, Integration of microfluidics with a four-channel integrated optical Young interferometer immunosensor, Biosens. Bioelectron. 20 (2005) 1417–1421.

[18] R. Gao, Y. Jiang, W. Ding, Z. Wang, D. Liu, Filmed extrinsic Fabry-Perot interferometric sensors for the measurement of arbitrary refractive index of liquid, Sens. Actuator B-Chem. 177 (2013) 924–928.

[19] N. Gaber, Y. Sabry, M. Erfan, F. Marty, T. Bourouina, High-Q FabryPérot Micro-Cavities for High-Sensitivity Volume Refractometry, Micromachines 9 (2018) 54.

[20] A. Leblanc-Hotte, J. S. Delisle, S. Lesage, Y.-A. Peter, The Importance of Single-Mode Behavior in Silicon-On-Insulator Rib Waveguides with Very Large Cross Section for Resonant Sensing Applications, IEEE J. Sel. Top. Quantum Electron. 22 (2016) 241–248.

[21] R. A. Flynn, B. Shao, M. Chachisvilis, M. Ozkan, S. C. Esener, Two-beam optical traps: Refractive index and size measurements of microscale objects, Biomed. Microdevices 7 (2005) 93–97.

[22] X. Liang, a.Q. Liu, C. Lim, T. Ayi, P. Yap, Determining refractive index of single living cell using an integrated microchip, Sens. Actuator A-Phys. 133 (2007) 349–354.

[23] W. Z. Song, X. M. Zhang, a. Q. Liu, C. S. Lim, P. H. Yap, H. M. M. Hosseini, Refractive index measurement of single living cells using on-chip Fabry-Perot cavity, Appl. Phys. Lett. 89 (2006) 203901.

[24] L. K. Chin, A. Q. Liu, C. S. Lim, X. M. Zhang, J. H. Ng, J. Z. Hao, S. Takahashi, Differential single living cell refractometry using grating resonant cavity with optical trap, Appl. Phys. Lett. 91 (2007) 89–92.

[25] P. Y. Liu, L. K. Chin, W. Ser, H. F. Chen, C.-M. Hsieh, C.-H. Lee, K.-B. Sung, T. C. Ayi, P. H. Yap, B. Liedberg, K. Wang, T. Bourouina, Y. Leprince-Wang, Cell refractive index for cell biology and disease diagnosis: past, present and future., Lab chip 16 (2016) 634–644.

[26] W. Wang, D. W. Kisker, D. H. Thamm, H. Shao, K. L. Lear, Optofluidic intracavity spectroscopy of canine hemangiosarcoma., IEEE Trans. Biomed. Eng. 58 (2011) 853–60.

[27] R. St-Gelais, J. Masson, Y.-A. Peter, All-silicon integrated FabryPerot cavity for volume refractive index measurement in microfluidic systems, Appl. Phys. Lett. 94 (2009) 243905.

[28] R. St-Gelais, A. Poulin, Y.-A. Peter, Advances in Modeling , Design, and Fabrication of Deep-Etched Multilayer Resonators, J. Lightwave Technol. 30 (2012) 1900–1908.

[29] J. Zhou, I. Papautsky, Fundamentals of inertial focusing in microchannels., Lab Chip 13 (2013) 1121–32.

[30] W. Lee, H. Amini, H. A. Stone, D. Di Carlo, Dynamic self-assembly and control of microfluidic particle crystals., Proc. Natl. Acad. Sci. USA 107 (2010) 22413–8.

[31] A. Leblanc-Hotte, J.-s. Delisle, S. Lesage, Y.-a. Peter, Optofluidic device for high resolution and multiparametric measurement of single biological cells, in: Solid-State Sensors, Actuators and Microsystems Workshop, Hilton Head Island, South Carolina, 2014, pp. 327–330.

[32] S. J. Collins, F. W. Ruscetti, R. E. Gallagher, R. C. Gallo, Terminal differentiation of human promyelocytic leukemia cells induced by dimethyl sulfoxide and other polar compounds, Proc. Natl. Acad. Sci. USA 75 (1978) 2458–2462.

[33] K. Muroi, R. Sasaki, Y. Miura, K. Ohyashiki, Medium pH determines the differentiation of human promyelocytic leukemia cells to basophils or eosinophils by culturing in a protein- and serum-free medium, Leuk. Res. 13 (1989) 157–163.

[34] H. Sun, S. Wang, Measuring the component overlapping in the Gaussian mixture model, Data Min. Knowl. Discov. 23 (2011) 479–502.

[35] K. Fukunaga, Introduction to statistical pattern recognition, second ed., Morgan Kaufmann, San Francisco, 1990.